Space-time discontinuous Galerkin finite element method for shallow water flows

V.R. Ambati *, O. Bokhove

Numerical Analysis and Computational Mechanics Group, P.O. Box 217, Department of Applied Mathematics, University of Twente, Enschede, The Netherlands

Abstract

A space-time discontinuous Galerkin (DG) finite element method is presented for the shallow water equations over varying bottom topography. The method results in non-linear equations per element, which are solved locally by establishing the element communication with a numerical HLLC flux. To deal with spurious oscillations around discontinuities, we employ a dissipation operator only around discontinuities using Krivodonova's discontinuity detector. The numerical scheme is verified by comparing numerical and exact solutions, and validated against a laboratory experiment involving flow through a contraction. We conclude that the method is second order accurate in both space and time for linear polynomials.

Key words: Shallow water equations, Discontinuous Galerkin finite element methods, Discontinuity detector, Numerical dissipation
PACS: 35L65, 65M60

1 Introduction

The shallow water equations including topographic effects are a leading order model to study coastal hydrodynamics on several scales including intermediate scale rotational waves (100 km range), and coastal currents and breaking waves

* Corresponding author.
Email addresses: v.r.ambati@math.utwente.nl (V.R. Ambati), o.bokhove@math.utwente.nl (O. Bokhove).

on beaches (meter to km range). The shallow water model, in the absence of discontinuities, conserves potential vorticity, enstrophy and energy; and captures many interesting natural wave phenomena in shallow water like flooding and drying at beaches, and hurricane-induced waves approaching coastal zones and tsunamis.

In this paper, we present a space-time discontinuous Galerkin finite element method for the (depth-averaged) shallow water equations. This numerical method has been developed by Van der Vegt and Van der Ven [11] to accurately model inviscid compressible flows in a time dependent flow domain. The method discretizes and solves the shallow water model locally per space-time finite element by establishing the element communication through a numerical HLLC flux in the spatial direction and a numerical upwind flux in the time direction. The numerical discretization results in a set of coupled nonlinear equations which can be solved efficiently and locally, by adding a pseudo-time derivative and integrating them using a Runge-Kutta scheme until the solution reaches steady state in pseudo-time. To improve the convergence acceleration, a multi-grid technique for pseudo-time integration scheme is proposed in [11]. However, we leave the multi-grid technique for future implementation.

The nonlinear shallow water equations can develop discontinuities in the form of bores or hydraulic jumps in finite time. To limit spurious oscillations around discontinuities, we employ a dissipation operator [4] but only around discontinuities using discontinuity detection scheme of Krivodonova et al. [5]. New in the present paper is the application of space-time DG method to shallow water flows combined with the localized application of numerical dissipation around bores or jumps. Furthermore, we verify the method for linear polynomials to show that it is second order accurate in space and time, and validate the method qualitatively with an interesting laboratory experiment.

2 Shallow water equations

Shallow water equations (see [7]) over a varying bottom topography can be concisely given in the index notation as

$$\nabla \cdot \mathcal{F}_i(\mathbf{U}) = S_i \text{ in a domain } \Omega, \tag{1}$$

where $\nabla = (\partial_t, \partial_x, \partial_y)$ is the differential operator, $\mathbf{U} = (h, hu, hv)$ the state vector, $h(\mathbf{x})$ the water depth, $\mathbf{u}(\mathbf{x}) = (u(\mathbf{x}), v(\mathbf{x}))$ the velocity field,

$$\mathcal{F}_i(\mathbf{U}) = \begin{pmatrix} h & hu & hv \\ hu & hu^2 + gh^2/2 & huv \\ hv & huv & hv^2 + gh^2/2 \end{pmatrix} \text{ and } S_i = \begin{pmatrix} 0 \\ -gh\partial_x h_b \\ -gh\partial_y h_b \end{pmatrix} \quad (2)$$

the flux and source vector, g the gravitational acceleration, $h_b(x, y)$ the bottom topography and $\mathbf{x} = (t, x, y)$. Finally, we complete the system (1) with inflow, outflow or solid wall boundary conditions and initial conditions $\mathbf{U}(0, x, y)$. The nonlinear shallow water equations (1) are hyperbolic and hence its solutions may develop discontinuities such as bores or hydraulic jumps. These discontinuities are weak solutions of shallow water equations, and satisfy Rankine-Hugoniot relations (see [10]) and energy dissipating conditions for uniqueness (see [6]).

3 Space-time discontinuous Galerkin method

3.1 Geometry of Space-time elements and Tessellation

The space-time flow domain $\mathcal{E} \in \mathbb{R}^3$ is defined as the open set of space-time points in the time interval (t_0, T)

$$\mathcal{E} := \{(t, \bar{x}) | \bar{x} \in \Omega, t_0 < t < T\} \subset \mathbb{R}^3 \quad (3)$$

with $\Omega \in \mathbb{R}^2$ the spatial domain, t_0 the initial time and T the final time. To tessellate the space-time domain, the time interval (t_0, T) will be divided into finite time intervals $I_n = [t_n, t_{n+1}]$ with $n = 0, \ldots, N_T$ and N_T the number of space-time slabs. Now at each time level t_n, we divide the spatial flow domain using the open space element K_{k}^n with closure $\bar{K}_{\mathsf{k}}^n$ to form a tessellation of N_e spatial elements. The tessellation of the spatial domain is

$$\bar{\mathcal{T}}_{\mathsf{h}} := \{K_{\mathsf{k}}^n | \bigcup_{\mathsf{k}=1}^{N_e} \bar{K}_{\mathsf{k}}^n = \bar{\Omega}_{\mathsf{h}} \text{ and } K_{\mathsf{k}}^n \cap K_{\mathsf{k}'}^n = \emptyset \text{ if } \mathsf{k} \neq \mathsf{k}', 1 \leq \mathsf{k}, \mathsf{k}' \leq N_e\}, \quad (4)$$

such that the computational space domain $\Omega_{\mathsf{h}} \to \Omega$ as $\mathsf{h} \to 0$, in which h is the smallest radius of radii of the largest circle completely containing element $K_{\mathsf{k}}^n \in \bar{\mathcal{T}}_{\mathsf{h}}$. Thus, the space-time tessellation consists of space-time elements $\mathcal{K}_{\mathsf{k}}^n$ which are obtained by connecting the corresponding spatial elements K_{k}^n and K_{k}^{n-1} of the computational space domain Ω_{h} at t_n and t_{n-1}. In the present work, the spatial flow domain is fixed in time and hence the corresponding

spatial elements K_{k}^n and K_{k}^{n-1} are identical. Hereafter, we thus drop the superscripts of the spatial elements.

Each spatial element K_{k} is mapped to a reference element $\hat{K}$ and its mapping $F_K : K_{\mathsf{k}} \mapsto \hat{K}$ is defined as

$$F_K : K_{\mathsf{k}} \mapsto \hat{K} : \bar{\zeta} \mapsto \bar{\mathbf{x}} := \sum_{\mathsf{j}} \bar{\mathbf{x}}_{\mathsf{j}} \; \chi_{\mathsf{j}}(\bar{\zeta}) \tag{5}$$

with $\bar{\zeta} = (\zeta_1, \zeta_2)$ the reference coordinates, $\bar{\mathbf{x}} = (x, y)$ the spatial coordinates and $\chi_{\mathsf{j}}(\bar{\zeta})$ the standard shape functions. Subsequently, the space-time element $\mathcal{K}_{\mathsf{k}}^n$ is mapped to a reference element $\hat{\mathcal{K}}$ and its mapping is defined as

$$G_{\mathcal{K}}^n : \mathcal{K}_{\mathsf{k}}^n \mapsto \hat{\mathcal{K}} : \zeta \mapsto \mathbf{x} := \Big(\frac{1}{2}\Big((t_n + t_{n-1}) + \zeta_0 (t_n - t_{n-1}) \Big), F_K(\bar{\zeta}) \Big) \tag{6}$$

with $\zeta = (\zeta_0, \bar{\zeta})$ the reference coordinates.

In the space-time tessellation, each space-time element is either connected to another space-time element through an interior face $\mathcal{S}_{\mathsf{m}} \in \Gamma_{int}$ or to the boundary through a boundary face $\mathcal{S}_{\mathsf{m}} \in \Gamma_{bou}$. The union of interior and boundary faces is $\Gamma = \Gamma_{int} \cup \Gamma_{bou}$. Each interior face $\mathcal{S}_{\mathsf{m}}$ is connected to the elements $\mathcal{K}^l$ and $\mathcal{K}^r$ and each boundary face is connected to an element $\mathcal{K}^l$. Since the spatial flow domain is fixed in time, all these faces are either parallel or perpendicular to the time axis.

3.2 Function spaces and traces

To define the discontinuous Galerkin weak formulation, we introduce the broken space $\mathcal{V}_{\mathsf{h}}^d$ defined as

$$\mathcal{V}_{\mathsf{h}}^d := \{ \mathbf{V}_{\mathsf{h}} \in L^1(\mathcal{K}^n) \Big| \mathbf{V}_{\mathsf{h}}|_{\mathcal{K}} \in (P^1(\mathcal{K}))^d \} \tag{7}$$

with P^1 the space of linear polynomials, L^1 the space of Lebesgue integrable functions, $d = \dim(\mathbf{V}_{\mathsf{h}})$ and $\mathbf{V}_{\mathsf{h}}$ the polynomial approximation per space-time element defined as

$$\mathbf{V}_{\mathsf{h}} := \sum_m \hat{\mathbf{V}}_m \, \psi_m(\mathbf{x}) \tag{8}$$

with $\hat{\mathbf{V}}_m$ the expansion coefficients and $\psi_m(\mathbf{x})$ the polynomial basis functions. To define the basis functions $\psi_m(\mathbf{x})$, we first define a set of polynomial basis functions $\hat{\phi}_m(\zeta)$ in the reference element $\hat{\mathcal{K}}$. For linear polynomials, we choose $\hat{\phi}_m$ as $(1,\ \zeta_0,\ \zeta_1,\ \zeta_2,\ \zeta_1\ \zeta_2)$. Using the mapping $G_{\mathcal{K}}^n$, we can transform the basis functions $\hat{\phi}_m(\zeta)$ on to each finite element $\mathcal{K}_{\mathsf{k}}^n$ as $\phi_m : \mathcal{K}_{\mathsf{k}}^n \to \mathbb{R}$. To split

the functions defined in the space-time element $\mathcal{K}^n_{\mathsf{k}}$ into element means and fluctuating part at $t_n^- := \lim_{\epsilon \uparrow 0}(t_n + \epsilon)$, we redefine the basis functions as

$$\psi_m(\mathbf{x}) : \mathcal{K}^n_{\mathsf{k}} \to \mathbb{R} := \begin{cases} 1 & m = 0 \\ \phi_m(\mathbf{x}) - \frac{1}{|K_{\mathsf{k}}|} \int_{K_{\mathsf{k}}} \phi_m(\mathbf{x}) \, \mathrm{d}K & \text{otherwise} \end{cases} \tag{9}$$

with $|K_{\mathsf{k}}| = \int_{K_{\mathsf{k}}} dK$ the area of the element K_{k}. Since $\mathbf{V}_{\mathsf{h}} \in \mathcal{V}^d_{\mathsf{h}}$, *i.e.,* the functions are approximated per space-time element $\mathcal{K}^n_{\mathsf{k}}$, the traces of the functions on each face from left and right elements are not equal and hence the traces are discontinuous. The trace of the function $\mathbf{V}_{\mathsf{h}}$ on the element boundary $\partial\mathcal{K}^n_{\mathsf{k}}$ from inside the space-time element $\mathcal{K}^n_{\mathsf{k}}$ is defined as

$$\mathbf{V}_{\mathsf{h}}(\mathbf{x})|_{\partial\mathcal{K}^n_{\mathsf{k}}} = \mathbf{V}^- := \lim_{\epsilon \uparrow 0} \mathbf{V}_{\mathsf{h}}(\mathbf{x} + \epsilon \mathbf{n}_{\mathcal{K}}) \tag{10}$$

with $\mathbf{n}_{\mathcal{K}}$ as the outward unit normal vector of the boundary $\partial\mathcal{K}^n_{\mathsf{k}}$.

3.3 Discontinuous Galerkin weak formulation

The discontinuous Galerkin weak formulation is obtained by multiplying the shallow water equations (1) with test function $\mathbf{W}_{\mathsf{h}} \in \mathcal{V}^d_{\mathsf{h}}$, integrating by parts over each space-time element $\mathcal{K}^n_{\mathsf{k}}$, using Gauss' theorem in space and time, and introducing the shorthand notation $\mathcal{F}_i^- = \mathcal{F}_i(\mathbf{U}^-)$.
Find a $\mathbf{U}_{\mathsf{h}} \in \mathcal{V}^d_{\mathsf{h}}$ *such that for all* $\mathbf{W}_{\mathsf{h}} \in \mathcal{V}^d_{\mathsf{h}}$

$$\int_{\partial\mathcal{K}^n_{\mathsf{k}}} \mathbf{n}_{\mathcal{K}} \cdot (W_i^- \mathcal{F}_i^-) \mathrm{d}(\partial\mathcal{K}) - \int_{\mathcal{K}^n_{\mathsf{k}}} \nabla W_{\mathsf{h}i} \cdot \mathcal{F}_i(\mathbf{U}_{\mathsf{h}}) \, \mathrm{d}\mathcal{K} - \int_{\mathcal{K}^n_{\mathsf{k}}} W_{\mathsf{h}i} \, S_i \, \mathrm{d}\mathcal{K} = 0 \tag{11}$$

is satisfied.
Summing the weak formulation (11) over all space-time elements $\mathcal{K}^n_{\mathsf{k}}$ in the space-time slab I_n and rearranging the summation of element boundary integrals into a summation of interior face integrals and boundary face integrals, we get

$$\begin{aligned} &\sum_{\mathcal{S}} \Big\{ \int_{\mathcal{S}_{\mathsf{m}} \in \Gamma_{int}} \Big(W_j^l (\mathbf{n}_{\mathcal{K}}^l \cdot \mathcal{F}_i^l) + W_j^r (\mathbf{n}_{\mathcal{K}}^r \cdot \mathcal{F}_i^r) \Big) \, \mathrm{d}\mathcal{S} + \int_{\mathcal{S}_{\mathsf{m}} \in \Gamma_{bou}} W_j^l (\mathbf{n}_{\mathcal{K}}^l \cdot \mathcal{F}_i^l) \, \mathrm{d}\mathcal{S} \Big\} - \\ &\sum_{\mathcal{K}} \Big\{ \int_{\mathcal{K}^n_{\mathsf{k}}} \nabla W_{\mathsf{h}j} \cdot \mathcal{F}_i(\mathbf{U}_{\mathsf{h}}) \, \mathrm{d}\mathcal{K} + \int_{\mathcal{K}^n_{\mathsf{k}}} W_{\mathsf{h}j} \, S_i \, \mathrm{d}\mathcal{K} \Big\} = 0, \end{aligned} \tag{12}$$

where $\mathbf{n}_{\mathcal{K}}^K$ is the outward unit normal vector of the face S_{m} w.r.t element $\mathcal{K}^K, K = l$ or r; and $\mathcal{F}^K$ and $\mathbf{U}^K$ are the limiting trace values on the face S_{m} from the element $\mathcal{K}^K, K = l$ or r. The flux term in the interior face integrals

(12) can be rewritten as follows:

$$W_i^l(\mathbf{n}_\mathcal{K}^l \cdot \mathcal{F}_i^l) + W_i^r(\mathbf{n}_\mathcal{K}^r \cdot \mathcal{F}_i^r) = (\alpha\mathcal{F}_i^l + \beta\mathcal{F}_i^r) \cdot (\mathbf{n}_\mathcal{K}^l W_i^l + \mathbf{n}_\mathcal{K}^r W_i^r) + (\mathbf{n}_\mathcal{K}^l \cdot \mathcal{F}_i^l + \mathbf{n}_\mathcal{K}^r \cdot \mathcal{F}_i^r)(\beta W_i^l + \alpha W_i^r) \tag{13}$$

with $\alpha, \beta > 0$ and $\alpha + \beta = 1$. If we enforce the continuity of the flux $\mathbf{n}_\mathcal{K}^l \cdot \mathcal{F}_i^l = -\mathbf{n}_\mathcal{K}^r \cdot \mathcal{F}_i^r$ and introduce a consistent and conservative numerical flux as $\tilde{\mathcal{F}}_i(\mathbf{U}^l, \mathbf{U}^r, \mathbf{n}_\mathcal{K}) \approx (\alpha\mathcal{F}_i^l + \beta\mathcal{F}_i^r)$ then the flux term (13) reduces to

$$W_i^l(\mathbf{n}_\mathcal{K}^l \cdot \mathcal{F}_i^l) + W_i^r(\mathbf{n}_\mathcal{K}^r \cdot \mathcal{F}_i^r) \approx (\mathbf{n}_\mathcal{K}^l \cdot \tilde{\mathcal{F}}_i(\mathbf{U}^l, \mathbf{U}^r, \mathbf{n}_\mathcal{K}))(W_i^l - W_i^r). \tag{14}$$

We also apply the boundary conditions through the numerical flux as $\tilde{\mathcal{F}}_i(\mathbf{U}^l, \mathbf{U}^b, \mathbf{n}_\mathcal{K})$ with $\mathbf{U}^b$ as the boundary condition. After introducing the numerical flux into the weak formulation (12), we obtain
Find a $\mathbf{U}_\mathsf{h} \in \mathcal{V}_\mathsf{h}^d$ *such that for all* $\mathbf{W}_\mathsf{h} \in \mathcal{V}_\mathsf{h}^d$

$$\sum_\mathcal{S}\Big\{ \int_{\mathcal{S}_\mathsf{m}} (\mathbf{n}_\mathcal{K}^l \cdot \tilde{\mathcal{F}}_i(\mathbf{U}^l, \mathbf{U}^r, \mathbf{n}_\mathcal{K}))(W_i^l - W_i^r)\, \mathrm{d}\mathcal{S} - \sum_\mathcal{K}\Big\{ \int_{\mathcal{K}_\mathsf{k}^n} \nabla W_{\mathsf{h}j} \cdot \mathcal{F}_i(\mathbf{U}_\mathsf{h})\, \mathrm{d}\mathcal{K} + \int_{\mathcal{K}_\mathsf{k}^n} W_{\mathsf{h}j}\, S_i\, \mathrm{d}\mathcal{K}\Big\} = 0 \tag{15}$$

is satisfied.
In (15), we have combined the interior and boundary face integrals by keeping in mind that $\mathbf{U}^r = \mathbf{U}^b$ and $W_i^r = 0$ when $\mathcal{S}_\mathsf{m} \in \Gamma_{bou}$. The numerical flux $\tilde{\mathcal{F}}_i(\mathbf{U}^l, \mathbf{U}^r, \mathbf{n}_\mathcal{K})$ through the faces is HLLC flux (see [3]) in spatial direction and upwind flux (see [11]) in time direction.

3.4 Local application of numerical dissipation around bores or jumps

Spurious oscillations appear around discontinuities or sharp gradients of the solutions of weak formulation (15). To suppress spurious oscillations, Van der Vegt and Van der Ven [11] introduced the following numerical dissipation operator into the weak formulation per space time element $\mathcal{K}_\mathsf{k}^n$:

$$\mathcal{D}_\mathsf{k}^n(\mathbf{U}_\mathsf{h}, \mathbf{U}_\mathsf{h}^*) := \int_{\mathcal{K}_\mathsf{k}^n} (\nabla W_{\mathsf{h}j})\, \mathfrak{D}_\mathsf{k}^n(\mathbf{U}_\mathsf{h}, \mathbf{U}_\mathsf{h}^*)\, (\nabla U_{\mathsf{h}i})^T\, \mathrm{d}\mathcal{K}, \tag{16}$$

where $\mathfrak{D}_\mathsf{k}^n(\mathbf{U}_\mathsf{h}, \mathbf{U}_\mathsf{h}^*)$ is the dissipation matrix which will be defined later, $\mathbf{U}_\mathsf{h}$ the solution in $\mathcal{K}_\mathsf{k}^n$ and $\mathbf{U}_\mathsf{h}^*$ the solution in the immediate neighboring elements of $\mathcal{K}_\mathsf{k}^n$. The dissipation operator (16) acts in every space-time element $\mathcal{K}_\mathsf{k}^n$ but is only required around discontinuities or sharp gradients.

Krivodonova et al. [5] proposed a discontinuity detection scheme such that the numerical dissipation operator (16) is applied only in the non-smooth regions.

The discontinuity detector for the shallow water equations can be defined as

$$\mathcal{I}_{\mathsf{k}}^{n}(h_{\mathsf{h}}, h_{\mathsf{h}}^{*}) := \frac{\sum\limits_{\mathcal{S}_m \in \partial\mathcal{K}_{\mathsf{k}}^{n}} \int_{\mathcal{S}_m} |h^{+} - h^{-}| \mathrm{d}\mathcal{S}}{\mathsf{h}_{\mathcal{K}}^{(p+1)/2} \, |\partial\mathcal{K}_{\mathsf{k}}^{n}| \, \max\|h_{\mathsf{h}}\|}, \tag{17}$$

where h_{h} is the approximated water depth, $\mathsf{h}_{\mathcal{K}}$ the cell measure defined as the radius of the largest circumscribed circle in the element $\mathcal{K}_{\mathsf{k}}^{n}$, $|\partial\mathcal{K}_{\mathsf{k}}^{n}|$ the surface area of the element, and $\max\|\cdot\|$ the maximum norm based on the local Gauss' integration points in the element $\mathcal{K}_{\mathsf{k}}^{n}$. Now the space-time elements in non-smooth and smooth regions are detected by $\mathcal{I}_{\mathsf{k}}^{n} > 1$ and $\mathcal{I}_{\mathsf{k}}^{n} < 1$, respectively.

The weak formulation (15) is combined with the dissipation operator (16) based on the scheme of discontinuity detector (17) as follows:
Find a $\mathbf{U}_{\mathsf{h}} \in \mathcal{V}_{\mathsf{h}}^{d}$ *such that for all* $\mathbf{W}_{\mathsf{h}} \in \mathcal{V}_{\mathsf{h}}^{d}$

$$\begin{aligned}
&\sum_{\mathcal{S}} \Big\{ \int_{\mathcal{S}_{\mathsf{m}}} (\mathbf{n}_{\mathcal{K}}^{l} \cdot \tilde{\mathcal{F}}_i(\mathbf{U}^{l}, \mathbf{U}^{r}, \mathbf{n}_{\mathcal{K}}))(W_i^{l} - W_i^{r}) \, \mathrm{d}\mathcal{S} - \\
&\sum_{\mathcal{K}} \Big\{ \int_{\mathcal{K}_{\mathsf{k}}^{n}} \nabla W_{\mathsf{h}j} \cdot \mathcal{F}_i(\mathbf{U}_{\mathsf{h}}) \, \mathrm{d}\mathcal{K} + \int_{\mathcal{K}_{\mathsf{k}}^{n}} W_{\mathsf{h}j} \, S_i \, \mathrm{d}\mathcal{K} - \Theta(\mathcal{I}_{\mathsf{k}}^{\mathrm{n}} - 1) \mathcal{D}_{\mathsf{k}}^{\mathrm{n}}(\mathbf{U}_{\mathsf{h}}, \mathbf{U}_{\mathsf{h}}^{*}) \Big\} = 0
\end{aligned} \tag{18}$$

is satisfied with $\Theta(\mathcal{I}_{\mathsf{k}}^{n} - 1)$ *the Heaviside function.*

3.5 Definition of dissipation matrix

The definition of the dissipation matrix, as in [11], is more straight forward in the reference coordinate directions than in the physical space-time coordinates, so we transform the dissipation matrix $\mathfrak{D}_{\mathsf{k}}^{n}(\mathbf{U}_{\mathsf{h}}, \mathbf{U}_{\mathsf{h}}^{*})$ to the reference coordinates using the relation

$$\mathfrak{D}_{\mathsf{k}}^{n}(\mathbf{U}_{\mathsf{h}}, \mathbf{U}_{\mathsf{h}}^{*}) = \mathfrak{R}^{T} \tilde{\mathfrak{D}}_{\mathsf{k}}^{n}(\mathbf{U}_{\mathsf{h}}, \mathbf{U}_{\mathsf{h}}^{*}) \mathfrak{R}, \tag{19}$$

where $\tilde{\mathfrak{D}}_{\mathsf{k}}^{n}(\mathbf{U}_{\mathsf{h}}, \mathbf{U}_{\mathsf{h}}^{*})$ is the dissipation matrix in reference coordinates, $\mathfrak{R}$ the rotation matrix defined as $\mathfrak{R} := 2\mathfrak{C}^{-1} \nabla G_{\mathcal{K}}^{n}$ with $\mathfrak{C} := \mathrm{diag}\{\mathsf{c}_0, \mathsf{c}_1, \mathsf{c}_2\}$ the diagonal matrix in which c_i, $i = 0 \ldots 2$ is the leading terms of the expansion of the mapping $G_{\mathcal{K}}^{n}$. Jaffre et al. [4] proposed a dissipation matrix $\tilde{\mathfrak{D}}_{\mathsf{k}}^{n}(\mathbf{U}_{\mathsf{h}}, \mathbf{U}_{\mathsf{h}}^{*})$ for hyperbolic conservation laws, which has been used by Van der Vegt and Van der Ven [11] for the compressible Euler equations. We adopt the dissipation model in [4] for shallow water equations as

$$\tilde{\mathfrak{D}}_{ij;\mathsf{k}}^{n} := \begin{cases} \max\Big(C_2 \mathsf{c}_{\mathcal{K}}^{2-\gamma} \mathcal{R}_{\mathsf{k}}^{n}(\mathbf{U}_{\mathsf{h}}, \mathbf{U}_{\mathsf{h}}^{*}), C_1 \mathsf{c}_{\mathcal{K}}^{1.5} \Big), & \text{if } \mathbf{W}_{\mathsf{h}} = \psi_m, \; m = 2, 3, 4 \\ 0, & \text{if } \mathbf{W}_{\mathsf{h}} = \psi_m, \; m = 0, 1, \end{cases} \tag{20}$$

with

$$\mathcal{R}^n_{\mathsf{k}}(\mathbf{U}_{\mathsf{h}}, \mathbf{U}^*_{\mathsf{h}}) := \max_i \left(\max_{\mathbf{x}\in\mathcal{K}^n_{\mathsf{k}}} \|\nabla \cdot \mathcal{F}_i(\mathbf{U}_{\mathsf{h}})\| \right) + \sum_{\mathcal{S}_{\mathsf{m}}\in\partial\mathcal{K}^n_{\mathsf{k}}} C_0 \max_i \left(\max_{\mathbf{x}\in\mathcal{S}_{\mathsf{m}}} \|\mathbf{n}^l_{\mathcal{K}} \cdot (\mathcal{F}^l_i - \mathcal{F}^r_i)\| / \mathsf{c}_{\mathcal{K}} \right), \tag{21}$$

$\mathsf{c}_{\mathcal{K}} = \sqrt{\mathsf{c}_0^2 + \mathsf{c}_1^2 + \mathsf{c}_2^2}$ the scaling factor, $\max\|\cdot\|$ is based on the maximum at the local Gauss integration points, and C_i, $i = 1 \ldots 2$, and γ are the positive constants. The positive constants are taken from [11] as $C_0 = 1.2$ if the normal of the face $\mathcal{S}_{\mathsf{m}}$ is parallel to the time direction or else $C_0 = 1.0$, and $\gamma = 0.1$ except $C_1 = 0.001$ and $C_2 = 0.001$ are tuned for shallow water equations.

3.6 Discretized weak formulation: nonlinear equations

The weak formulation (18) is discretized by substituting the polynomial approximation of the state vector $\mathbf{U}_{\mathsf{h}}$ and using the arbitrariness of the test function $\mathbf{W}_{\mathsf{h}}$. Firstly, we choose the test function $W_{\mathsf{h}j} = 1$ to obtain a discretized equation for means $\hat{\mathbf{U}}_0$ as

$$\sum_{\mathcal{S}\in\mathcal{K}^n_{\mathsf{k}}} \left\{ \int_{\mathcal{S}_{\mathsf{m}}} \mathbf{n}_{\mathcal{K}} \cdot \tilde{\mathcal{F}}_i(\mathbf{U}^l, \mathbf{U}^r, \mathbf{n}_{\mathcal{K}}) \, \mathrm{d}\mathcal{S} \right\} - \int_{\mathcal{K}^n_{\mathsf{k}}} S_i \, \mathrm{d}\mathcal{K} = 0 \tag{22}$$

Secondly, we choose the test function $W_{\mathsf{h}j} = \psi_j$ to obtain discretized equations for slopes $\hat{\mathbf{U}}_j$ as

$$\sum_{\mathcal{S}\in\mathcal{K}^n_{\mathsf{k}}} \left\{ \int_{\mathcal{S}_{\mathsf{m}}} \left(\mathbf{n}_{\mathcal{K}} \tilde{\mathcal{F}}_i(\mathbf{U}^l, \mathbf{U}^r, \mathbf{n}_{\mathcal{K}}) \psi_j \, \mathrm{d}\mathcal{S} \right\} - \int_{\mathcal{K}^n_{\mathsf{k}}} \nabla\psi_j \cdot \mathcal{F}_i(\mathbf{U}_{\mathsf{h}}) \, \mathrm{d}\mathcal{K} \right.$$
$$\left. + \Theta(\mathcal{I}^n_{\mathsf{k}} - 1) \sum_{m=0}^{4} \hat{U}^n_{i,m} \int_{\mathcal{K}^n_{\mathsf{k}}} (\nabla\psi_j) \, \mathfrak{D}^n_{\mathsf{k}}(\mathbf{U}_{\mathsf{h}}, \mathbf{U}^*_{\mathsf{h}}) \, (\nabla\psi_m)^T \, \mathrm{d}\mathcal{K} - \int_{\mathcal{K}^n_{\mathsf{k}}} \psi_j \, S_i \, \mathrm{d}\mathcal{K} \right\} = 0, \tag{23}$$

with $j = 0, 1, \ldots, 4$ the index for basis equations; $i = 0, 1, 2$ the index for the shallow water equations and m the index for the expansion coefficients. The various terms in the the nonlinear equations (22) and (23) are represented as

follows:

$$
\begin{aligned}
E^n_{\mathsf{k};ij}(\hat{\mathbf{U}}^n) &= \int_{\mathcal{K}^n_{\mathsf{k}}} \nabla\psi_j \cdot \mathcal{F}_i(\mathbf{U}_{\mathsf{h}})\,\mathrm{d}\mathcal{K},\\
F^{\mathsf{k};n}_{\mathcal{S};ij}(\hat{\mathbf{U}}^n, \hat{\mathbf{U}}^{n-1}) &= \int_{\mathcal{S}_{\mathsf{m}}\in\mathcal{K}^n_{\mathsf{k}}} \mathbf{n}_{\mathcal{K}} \cdot \tilde{\mathcal{F}}_i(\mathbf{U}^l, \mathbf{U}^r, \mathbf{n}_{\mathcal{K}})\psi_j\,\mathrm{d}\mathcal{S},\\
D^n_{\mathsf{k};ij}(\hat{\mathbf{U}}^n) &= \sum_{m=0}^{4} \hat{U}^n_{i,m}\bar{D}^n_{\mathsf{k};jm} \quad \text{with}\\
\bar{D}^n_{\mathsf{k};jm} &= \int_{\mathcal{K}^n_{\mathsf{k}}} (\nabla\psi_j)\,\mathfrak{D}^n_{\mathsf{k}}(\mathbf{U}_{\mathsf{h}}, \mathbf{U}^*_{\mathsf{h}})\,(\nabla\psi_m)^T\,\mathrm{d}\mathcal{K}, \quad \text{and}\\
G^n_{\mathsf{k};ij}(\hat{\mathbf{U}}^n) &= \int_{\mathcal{K}^n_{\mathsf{k}}} \psi_j\, S_i\,\mathrm{d}\mathcal{K}.
\end{aligned}
\tag{24}
$$

We thus obtain the non-linear set of equations (22) to (23) for each space-time element which are represented as

$$
L^n_{\mathsf{k};ij}(\hat{\mathbf{U}}^n, \hat{\mathbf{U}}^{n-1}) = \sum_{\mathcal{S}\in\mathcal{K}^n_{\mathsf{k}}} F^{\mathsf{k};n}_{\mathcal{S};ij} - E^n_{\mathsf{k};ij} + \Theta(\mathcal{I}^n_{\mathsf{k}} - 1)D^n_{\mathsf{k};ij} - G^n_{\mathsf{k};ij} = 0, \tag{25}
$$

where n represents the space-time level and k represents the index of the space-time element $\mathcal{K}^n_{\mathsf{k}}$. Given the coefficients $\hat{\mathbf{U}}^{n-1}$ at the previous time level t_{n-1} we have to find the coefficients $\hat{\mathbf{U}}^n$ at the present time level t_n satisfying (22) and (23).

3.7 Pseudo-time integration: nonlinear solver

To solve the system of nonlinear equations (25) obtained from space-time discontinuous Galerkin discretization we augment them with pseudo-time derivative as

$$
|K^n_{\mathsf{k}}|\frac{\partial\hat{U}_{i;j}}{\partial\tau} = \frac{1}{\Delta t}L^n_{\mathsf{k};ij}(\hat{\mathbf{U}}^n, \hat{\mathbf{U}}^{n-1}) \tag{26}
$$

with $\Delta t = (t_n - t_{n-1})$ time step and $|K^n_{\mathsf{k}}| = |\mathcal{K}^n_{\mathsf{k}}|/\Delta t$. Now we integrate (26) until the solution reaches steady state in pseudo-time, *i.e.,*

$$
L^n_{\mathsf{k};ij}(\hat{\mathbf{U}}^n, \hat{\mathbf{U}}^{n-1}) \approx 0. \tag{27}
$$

The pseudo-time integration scheme is obtained from a second order accurate five stage Runge-Kutta scheme by treating $\hat{\mathbf{V}}$ in $L^n_{\mathsf{k}}(\hat{\mathbf{V}}, \hat{\mathbf{U}}^{n-1})$ semi-implicitly

as

$$\left(I + \frac{\alpha_s \lambda}{|K_{\mathsf{k}}^n|}\Big(|K_{\mathsf{k}}^n| I + \Theta(\mathcal{I}_{\mathsf{k}}^n - 1)\bar{D}_{\mathsf{k}}^n\Big)\right)\hat{\mathbf{V}}^s =$$

$$\hat{\mathbf{V}}^0 + \frac{\alpha_s \lambda}{|K_{\mathsf{k}}^n|}\left(\Big(|K_{\mathsf{k}}^n| I + \Theta(\mathcal{I}_{\mathsf{k}}^n - 1)\bar{D}_{\mathsf{k}}^n\Big)\hat{V}_{ij}^{s-1} - L_{\mathsf{k};ij}^n(\hat{\mathbf{V}}^{s-1},\ \hat{\mathbf{U}}^{n-1})\right). \quad (28)$$

where $s = 1, \ldots, 5$ are the Runge-Kutta stages, $\alpha_s = (0.0791451,\ 0.163551,\ 0.283663,\ 0.5,\ 1.0)$ the Runge-Kutta coefficients, $\lambda = \Delta\tau/\Delta t$ and $\Delta\tau$ the pseudo-time step. The pseudo-time step $\Delta\tau$ is determined locally per space-time element by a CFL condition given as

$$\Delta\tau|_{\mathcal{K}_{\mathsf{k}}^n} = \frac{\mathbf{CFL}_{\Delta\tau}|K^n|}{S_{\mathsf{k};\max}^n} \quad (29)$$

with $S_{\mathsf{k};\max}^n$ as the maximum wave speed in the space-time element $\mathcal{K}_{\mathsf{k}}^n$ and $\mathbf{CFL}_{\Delta\tau} = 0.8$ the CFL number for pseudo-time step.

In our numerical computations, we observed that in the presence of discontinuities some regions may oscillate between the smooth and non-smooth state resulting in non-converging scheme. Indeed, the residue $\max\|L_{\mathsf{k}}^n\|$ oscillates between two values. This is mainly due to the reason that the pseudo-time integration scheme (28) integrates the nonlinear system $(\bar{A}_{\mathsf{k}}^n + \bar{D}_{\mathsf{k}}^n)\hat{\mathbf{V}} = 0$, when $\mathcal{I}_{\mathsf{k}}^n > 1$ and $\bar{A}_{\mathsf{k}}^n\hat{\mathbf{V}} = 0$, otherwise per space-time element $\mathcal{K}_{\mathsf{k}}^n$. To avoid this, we use a switch $\mathcal{I}'^n_{\mathsf{k}}$ in every space-time element such that $\mathcal{I}'^n_{\mathsf{k}}$ is initialized with the value -1 at the beginning of the pseudo-time integration scheme and, $\mathcal{I}'^n_{\mathsf{k}}$ is switched to 1 when $\mathcal{I}_{\mathsf{k}}^n > 1$ and will remain unaltered after 4 or 5 pseudo-time steps until the solution reaches steady state in pseudo-time. Finally in the numerical scheme, we replace the $\Theta(\mathcal{I}_{\mathsf{k}}^n - 1)$ with $\Theta(\mathcal{I}'^n_{\mathsf{k}})$ to achieve convergence.

4 Verification

4.1 Burgers' solution

The one dimensional shallow water equations with $h_b = 0$ take the form of Burgers' equation $\partial_t q + q\partial_x q = 0$, when one of its Riemann invariants is taken constant such that $u + 2\sqrt{gh} = c$ with $q(x,t) = c - 3\sqrt{gh}$. An implicit exact solution can be constructed as

$$h(x,t) = (q(x,t) - c)^2/g \text{ and } u(x,t) = (c - 2q(x,t))/3 \quad (30)$$

with $q(x,t) = q_0(x^{'})$, $x = x^{'} + q_0(x^{'})t$ and $q(x,0) = q_0(x)$ the initial condition. Now for any given initial condition $q_0(x)$ with $dq_0/dx < 0$ somewhere, wave breaking occurs at time $t_b = -1/\min(dq_0/dx)$.

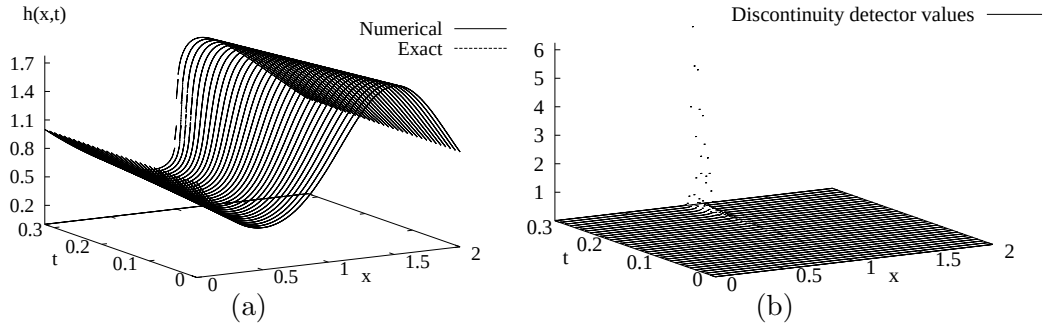

Fig. 1. a) Comparison of exact and numerical solutions of water depth $h(x,t)$ computed on a spatial mesh of 160×1 elements for Burgers' solution. b) Plot of the discontinuity detector on a spatial mesh of 160×1 elements showing clearly the smooth and discontinuous regions.

In our numerical simulation, we choose $c = 3$, $q_0(x) = sin(\pi x)$ with $x \in [0, 2]$ and use periodic boundary conditions along x. The space-time profile of water depth $h(x,t)$ for the exact and numerical solutions are shown in Figure 1(a) until wave breaking occurs. It should be observed from the numerical solution that the smooth initial condition develops into a discontinuity in a finite time $t < t_b = 1/\pi$. This helps us to test Krivodonova's discontinuity detector, which shows no sign of discontinuity in the beginning and gradually detects the regions with sharp gradients and finally detects discontinuities as shown in Figure 1(b). Before breaking, we compute the error $\|\mathsf{Error}\|_{\mathsf{L}^2(\Omega_\mathsf{h})} := (\int_{\Omega_\mathsf{h}}(\mathbf{U} - \mathbf{U}_\mathsf{h})^2 \mathrm{d}\Omega)^{1/2}$ for mass, h and momentum, hu on various meshes and plot them on a log-log scale as shown in Figure 2. The slope of the curve shows that the method is second order accurate in space.

4.2 Riemann problem

Consider the Riemann problem of the one dimensional shallow water equations with $h_b = 0$, the initial condition

$$\Big(h(x,0), u(x,0)\Big) = (h_L, u_L) \text{ if } x < x_0 \text{ and } (h_R, u_R) \text{ otherwise,} \tag{31}$$

and extrapolating boundary conditions. For the exact solution of Riemann problem we refer to [10]. We choose the initial condition $(h_L, u_L) = (0.09, 0.0)$ and $(h_R, u_R) = (0.02, 0.0)$ with a discontinuity at $x = 1.0$ in the domain $[0, 2]$, such that it gives rise to a left rarefaction and right shock wave. The numerical and exact space-time profile of the water depth $h(x,t)$ is shown in Figure 3(a) from $t = 0.0$ to 2.0. The space-time profile of the discontinuity detector, Figure

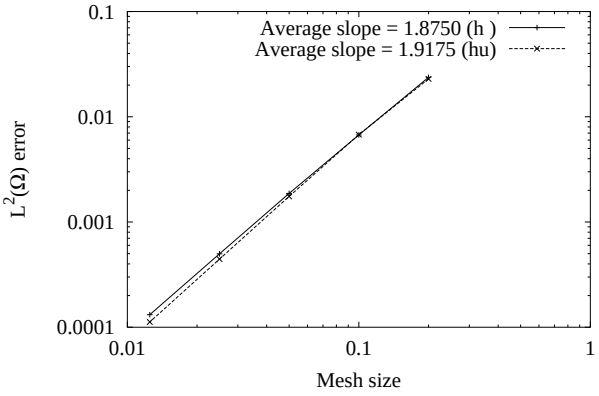

Fig. 2. Log-log plot of L^2 error versus mesh size. The L^2 error is computed on spatial meshes of size 10×1, 20×1, 40×1, 80×1 and 160×1 elements with time steps $\Delta t = 0.05, 0.025, 0.0125$ and 0.0625 at time $t = 0.2$.

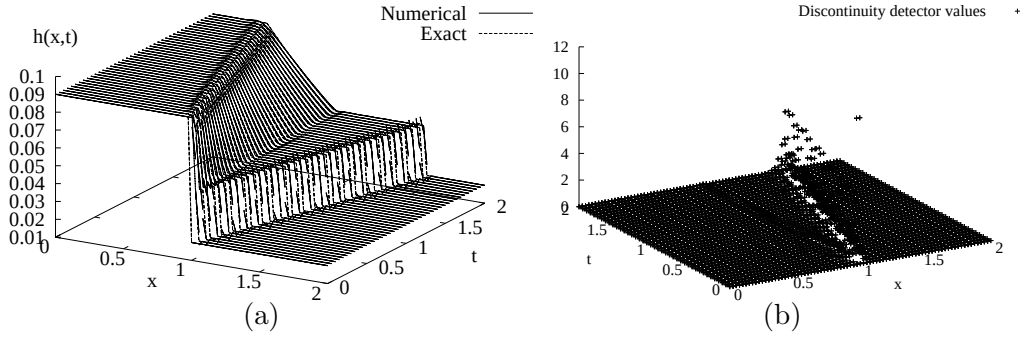

Fig. 3. a) Comparison of exact and numerical solutions of water depth $h(x,t)$ computed on a spatial mesh of 80×1 elements for the Riemann problem. b) Plot of discontinuity detector on a spatial mesh of 80×1 elements showing the smooth and discontinuous regions. Observe that the discontinuity detector is greater than one only near by the shock wave.

3(b), clearly illustrates that the dissipation is applied only around the shock wave and the spurious oscillations are limited.

5 Experimental validation

5.1 Flow through a contraction

Shallow water flows through a contraction can under certain flow rates and Froude numbers develop steady oblique hydraulic jumps. Akers [1] derived these steady state solutions and conducted laboratory experiments under different flow rates and Froude numbers. His experimental setup consisted of a narrow flume of length 150 cm. The width of the channel starts decreasing

linearly at 119.5 cm from 20 cm at the beginning of the contraction or inlet to 14 cm at the end of the flume or outlet. The steady state state shown in Figure 5.1(a) is reached experimentally with a constant inflow of water with depth h_0, u_0 such that the Froude number $F_0 = u_0/\sqrt{gh_0} = 3.65$. From the shock relations [9] for the shallow water system (1) and (2), the jump ratio and angle of the hydraulic jump can be calculated as steady state solutions. We find (Al-Tarazi et al. [2]) that

$$\frac{h_1}{h_0} = \frac{\tan\theta_s}{\tan(\theta_s - \theta_c)} \quad \text{and} \quad \sin\theta_s = \sqrt{\frac{1}{2F_0^2}\frac{h_1}{h_0}\left(1 + \frac{h_1}{h_0}\right)}, \tag{32}$$

where h_1 the height of the hydraulic jump, and θ_c and θ_s are the angle of the contraction and the jump measured relative to the horizontal wall of the flume. The two relations in (32) can be combined such that given the uniform upstream conditions u_0, h_0, F_0 and the angle θ_c of the contraction, we can entirely determine the conditions u_1, v_1, h_1, θ_s downstream of the oblique jumps. For increasing Froude numbers, the shocks cross within the contraction, the shallow water analogy of a Mach stem appears, and for even higher Froude numbers an upstream moving bore for:

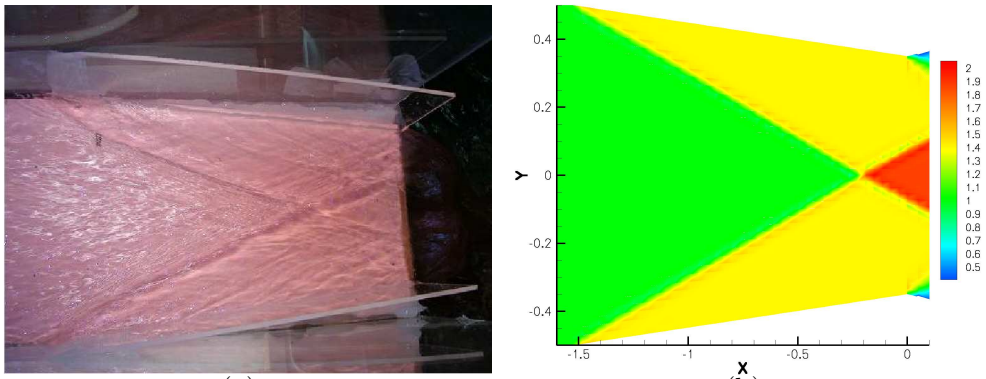

(a) (b)

Fig. 4. a) Experimental: Steady oblique hydraulic jumps formed in the contraction with jump ratio $h_1/h_0 = 1.8$, angle $\theta_s = 25.2°$ and Froude number $F_0 = 3.65$. b) Numerical: Intersecting hydraulic jumps formed in the contraction with non-dimensionalized parameters $u_0 = 1$, $h_0 = 1$, $H = 0.1$, $F_0 = 3.65$, $g = 1/F_0^2$. Observed jump ratio $h_1/h_0 = 1.4$ and angle $\theta_s = 20.54°$.

To achieve a steady state in our numerical simulation, we used a zero velocity and constant depth H as the initial conditions with inflow, outflow and solid wall boundary conditions. To mimic the experimental initial condition $H = 0$, we take $H \ll h_0$ due to which negative depths can occur numerically. The negative depths are corrected by setting the slopes of the approximated depth to zero. After some time, the effect of this correction vanishes and we achieve the steady oblique hydraulic jumps in our simulations with similar jump ratio and oblique jump angle qualitatively measured from the Figure 5.1(b).

6 Conclusions

Shallow water equations including topographic terms are discretized, verified and validated against a laboratory experiment with a space-time discontinuous Galerkin method. To avoid numerical oscillations around discontinuities, we applied numerical dissipation only at discontinuities which are effectively detected by Krivodonova et al.'s [5] discontinuity detector. Our numerical results are second order accurate for smooth exact solutions and show limited spurious oscillations in the presence of bores or jumps. We successfully validated the numerical shallow water code against laboratory data (Akers [1]) of oblique hydraulic jumps or "shocks" for hydraulic shallow flow through a contraction.

References

[1] B. Akers, Shallow water flow through a contraction, GFD Fellowship program 2005, Woods Hole Oceanographic Institution, 2005.

[2] M. Al-Tarazi, O. Bokhove, J.A.M. Kuipers, M. van Sint Annaland, A.W. Vreman, Reservoir formation in shallow granular flows through a contraction. Under revision *Phys. Rev. Lett.* (2005).

[3] O. Bokhove, Flooding and drying in finite-element Galerkin discretizations of shallow water equations. Part I: one dimension, *J. Sci. Comput.* **22** (2005) 47 - 82.

[4] J. Jaffre, C. Johnson, A. Szepessy, Convergence of the discontinuous Galerkin method for hyperbolic conservation laws, *Math. Models and Methods in Appl. Sci.* **5** (1995) 367-386.

[5] L. Krivodonova, J. Xin, J.-F. Remacle, N. Chevaugeon, J.E. Flaherty, Shock detection and limiting with discontinuous Galerkin methods for hyperbolic conservation laws, *Appl. Numer. Math.* **48** (2004) 323-338.

[6] H. Lamb, *Hydrodynamics*, Dover Publications, New York, 1932.

[7] J. Pedlosky, *Geophysical fluid dynamics*, Springer, New York, 1998.

[8] D.H. Peregrine, Surf zone currents, *Theoret. Comput. Fluid Dynamics* **10** (1998) 295-309.

[9] A.H. Shapiro, *The dynamics and thermodynamics of compressible fluid flow*, Ronald, New York, 1953.

[10] E.F. Toro, *Shock-capturing methods for free-surface flows*, Wiley, Toronto, 2001.

[11] J.J.W. Van der Vegt, H. Van der Ven, Space-time discontinuous Galerkin finite element method with dynamic grid motion for inviscid compressible flows, *J. Comput. Phys.* **182** (2002) 546-585.